Scilight

Photocatalysis

https://www.sciltp.com/journals/photocatalysis

Article

Controlling Photocatalytic Activity via a "Dual Role" Dopant: A Systematic Study of Fe-Doped TiO_2 Microspheres with Exposed {001} Facets

Jingxuan Wang [1], Jinan Niu [1,*], Jinpen Bao [1], Liuyun Huang [1], Deyuan Wang [2], Yifan Li [3] and Peizhong Feng [1,*]

[1] Mineral-Based Energy and Environment Materials Laboratory (ME² Lab), School of Materials Science and Physics, China University of Mining and Technology, Xuzhou 221116, China
[2] School of Computer Science and Technology, China University of Mining and Technology, Xuzhou 221116, China
[3] School of Mathematics, China University of Mining and Technology, Xuzhou 221116, China
* Correspondence: jinan.niu@cumt.edu.cn (J.N.); pzfeng@cumt.edu.cn (P.F.);
Tel.: +86-516-83591879 (J.N.); +86-516-83591877 (P.F.)

How To Cite: Wang, J.; Niu, J.; Bao, J.; et al. Controlling Photocatalytic Activity via a "Dual Role" Dopant: A Systematic Study of Fe-Doped TiO_2 Microspheres with Exposed {001} Facets. *Photocatalysis* **2025**, *1*(1), 1. https://doi.org/10.53941/photocatalysis.2025.100001

Received: 23 June 2025
Revised: 13 September 2025
Accepted: 24 September 2025
Published: 29 September 2025

Abstract: This work presents a facile hydrothermal method for synthesizing iron-doped anatase TiO_2 hierarchical microspheres composed of embedded single crystals with exposed {001} facets. In this approach, ferric fluoride (FeF_3) uniquely serves as both the iron source for doping and a morphology control agent. The influence of a wide range of Fe doping concentrations (from 2.23% to 20.13% atomic ratio) on the phase structure, morphology, optical properties, and photocatalytic activity was systematically investigated. The results show that at low doping levels (<15%), single-phase anatase microspheres are formed, with the constituent nanosheets becoming progressively thinner as the dopant amount increases. At higher concentrations, a phase transition occurs, yielding mixed phases of anatase and rutile (17.46% Fe) or rutile and an unidentified phase (20.13% Fe). Photocatalytic activity tests revealed that low Fe content (2.23% and 5.38%) enhanced the generation of hydroxyl radicals compared to undoped TiO_2, while higher concentrations led to decreased activity. This non-monotonic trend is attributed to the "dual role" of the iron dopant: (1) morphology control by fluoride ions, which increases the exposure of active {001} facets; (2) Fe-induced charge separation at low concentrations, which enhances carrier lifetime, and Fe-induced recombination centers at high concentrations, which diminishes photocatalytic efficiency. This work provides a novel strategy for precisely tuning the morphology and electronic structure of TiO_2 and offers insights into the complex role of dopants in photocatalysis.

Keywords: titanium dioxide; iron doping; photocatalysis; {001} facets; morphology control; ferric fluoride

1. Introduction

Titanium dioxide (TiO_2), particularly its anatase polymorph, is a cornerstone material in photocatalysis due to its stability, low cost, and non-toxicity [1–7]. However, two intrinsic limitations hinder its widespread application. The first is its wide bandgap (~3.2 eV), which restricts its photoactivity to the UV portion of the solar spectrum [8–11]. The second is that conventional synthesis often yields nanoparticles that are difficult to recover or thermodynamically stable crystals that primarily expose the less reactive {101} facets [12–15].

A significant breakthrough in addressing the facet issue came in 2008, when Yang et al. developed a method to synthesize anatase single crystals with a high percentage of exposed {001} facets [16]. These {001} facets, possessing a higher surface energy (~0.90 J/m^2) than the {101} facets (~0.44 J/m^2), exhibit far greater reactivity. This high activity stems from a greater density of undercoordinated titanium atoms, which serve as active sites for reactant adsorption and catalysis. While this facet engineering was a major advance, it did not solve the fundamental problem of the wide bandgap [17,18].

To enhance visible light utilization, the most common strategy is doping TiO_2 with foreign elements [19], with iron (Fe) being a particularly well-studied, cost-effective dopant [20–34]. Introducing Fe^{3+} into the TiO_2 lattice can significantly boost photocatalytic efficiency. This enhancement is twofold: it creates impurity energy levels that extend light absorption into the visible range, and the dopant sites act as charge traps. By capturing photo-excited electrons, these sites suppress the rapid recombination of electron-hole pairs, thereby increasing the quantum yield and the production of reactive oxygen species responsible for degrading organic pollutants.

Despite the clear advantages of both strategies, a significant research gap remains. While numerous methods—such as microemulsion, sol-gel, and impregnation—have been developed to produce Fe-doped TiO_2, these efforts have predominantly focused on nanoparticles or their aggregates [20–34]. Such materials often suffer from poor mechanical strength and are difficult to recycle. Reports on robust, Fe-doped anatase single crystals with dominant {001} facets remain exceptionally rare, and existing methods often rely on expensive precursors or complex reaction systems, limiting their practical application [35,36].

Herein, we address this challenge by presenting a facile and low-cost method for synthesizing Fe-doped anatase TiO_2 microspheres self-assembled from embedded single crystals with highly exposed {001} facets. Our key innovation is the use of FeF_3 as a novel, dual-function precursor that acts as both the iron source and a morphology-controlling agent [14]. This approach avoids introducing contaminating anions and promotes the formation of the desired high-energy facets [37,38]. We systematically investigate the effects of a wide range of Fe doping on the material's morphology, structure, and photoactivity, demonstrating a scalable path toward highly stable and efficient visible-light photocatalysts.

2. Experimental

2.1. Sample Preparation

All chemicals were used as received without further purification. P25 TiO_2 was purchased from Evonik Degussa Co., Ltd., FeF_3 (≥97%) was purchased from Alfa Aesar. Hydrofluoric acid (HF) (40 wt %), hydrogen peroxide (H_2O_2) (30 wt %), isopropanol (IPA, ≥99.7%), ammonium oxalate (AO, ≥99.8%), and benzoquinone (BQ, ≥99.0%) were all purchased from Sinopham (Shanghai).

Fe-doped samples were synthesized from TiO_2 powders by a facile route [39]. In a typical synthesis, 1 g TiO_2 powers, 40 mL water and 1 mL hydrofluoric acid were added into an 80 mL Teflon-lined autoclave and heated at 180 °C for 12 h. This step resulted in the dissolution of approximately 0.1 g of TiO_2, as determined by weighing the remaining undissolved material. Then a certain amount of FeF_3, 6 mL of the obtained precursor solution, 21 mL water, and 3 mL hydrogen peroxide were added into a 50 mL Teflon-lined autoclave and kept at 180 ℃ for 10 h. After allowing the autoclave to cool to room temperature, samples were collected by centrifugation, washed thoroughly with deionized water, and dried at 80 ℃. The as-obtained samples are denoted as S1, S2, S3, S4, S5 and S6 according to the corresponding amount of FeF_3, 0.001, 0.003, 0.006, 0.01, 0.02 and 0.04 g respectively (the ideal molar contents of Fe/(Fe + Ti) are 2.36%, 6.77%, 12.66%, 24%, 33.3% and 50%, and the actual results of ICP-OES detection are 2.23%, 5.38%, 9.75%, 14.35%, 17.46%, and 20.13%, respectively). In the control experiments, undoped TiO_2 was prepared in the same hydrothermal system without the addition of FeF_3, is denoted as S0; while akaganeite (FeOOH) was synthesized by using 6 mL of mixed solution of 40 mL water and 1 mL hydrofluoric acid as precursor, and 0.2 g FeF_3 as iron source, is denoted as S7.

2.2. Characterization

The crystal structure of the products was determined by X-ray diffraction (XRD, D8 Advance, Bruker, Germany) with Cu Kα radiation (λ = 1.54056 Å). Scanning electron microscope (SEM) images were taken with a field-emission SEM (FE-SEM, Sirion200, FEI, USA). X-ray photoelectron spectroscopy spectra (XPS) were recorded on Thermo Fisher ESCALAB 250Xi electron spectrometer with monochromatic Al Kα X-ray source (USA). The diffuse reflectance spectrum (DRS) were recorded on a UV-vis spectrophotometer (HR3000-Pro, Jingyi Electronic Science and Technology Co., Ltd., Guangzhou, China) with a integrating sphere in the range of 300–800 nm, and barium sulfate ($BaSO_4$) was used as a standard. The photoluminescence (PL) emission spectrum

of all the samples dispersed in water was recorded with excitation by incident light of 243 nm wavelength with a fluorescence spectrophotometer (Cary-Eclipse 500, Varian, USA) in the range of 300–600 nm. The content of Fe in samples was analyzed by inductively coupled plasma optical emission spectrometer (ICP-OES, 5110, Agilent, USA).

2.3. Evaluation of Photoactivity

The photocatalytic activity of the samples was evaluated by measuring the production of hydroxyl radicals (•OH) using terephthalic acid (TA) as a fluorescent probe. The measurement was carried out in the reaction chamber at 20 ℃ following the method reported in reference [40]. 10 mg samples were suspended in 40 mL of aqueous solution containing 0.01 M NaOH and 3.0 mM TA. Before exposure to UV-vis light irradiation, the suspension was stirred in the dark for 30 min. Then, 5.0 mL solution was taken out every 30 min, and the TiO_2 was separated from the solution with a centrifugation method. The remaining clear liquid was used for fluorescence spectrum measurements. The employed excitation light in recording fluorescence spectra was 320 nm and the widths of the excitation and emission slits were 10 nm. The light source employed in photoreactions was a 250 W mercury lamp (Shanghai Jiguang Special Lighting) with predominantly light at 365 nm wavelength. To gain information on the photocatalytic mechanism, a series of active species trapping experiments were performed. IPA was used to trap hydroxyl radicals (•OH), AO to quench holes (h^+), and BQ to capture superoxide ion ($•O^{2-}$). The concentration of each trapping agent is as follows: 10 mmol/L for IPA, 6 mmol/L for AO, and 0.1 mmol/L for BQ [41].

3. Results and Discussions

3.1. XRD Analysis

The crystal structure of as-prepared samples was investigated by means of XRD, as shown in Figure 1. It can be seen that when the amount of dopant is relatively small (S1–S4), the diffraction profiles are similar to that of undoped sample (S0) whose diffraction peaks are in good agreement with those of anatase (JCPDS card No. 21-1272). No significant impurities were detected in this doping range, which strongly suggests that the iron element was substitutionally incorporated into the TiO_2.

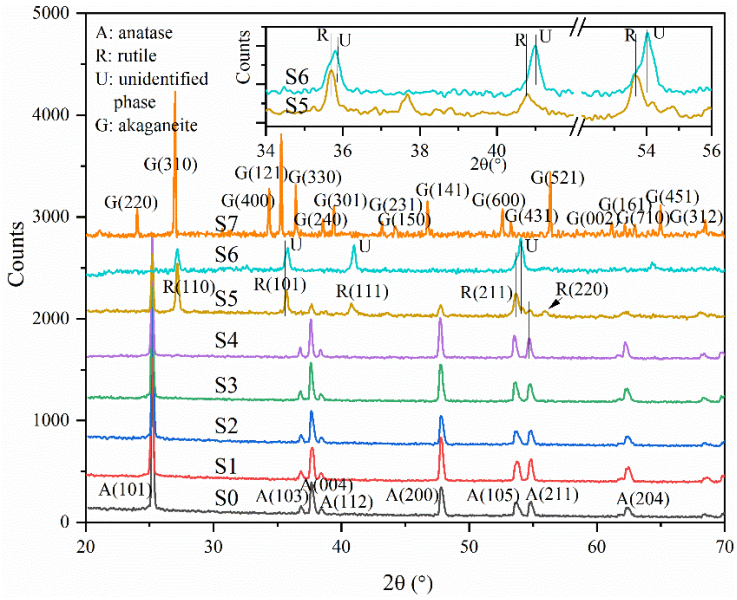

Figure 1. XRD patterns of Fe-doped samples S1–S6, pure TiO_2 sample (S0) and akaganeite sample (S7).

When Fe content increases to 17.46% (S5), rutile begins to be detected according to the JCPDS card of No. 21-1276 along with anatase. The similar phase change from anatase to rutile with increase of Fe content has been also found in many other studies [24,42–44], although the exact Fe content about the change is somewhat different, which can be attributed to the employment of different iron dopant. This result is significant because it not only further suggests that iron ions substitutionally replace Ti ions, but also indicates that the rutile phase, which forms at higher doping levels, can accommodate more iron than the anatase phase [24].

As Fe content reaches 20.13% (S6), anatase phase gradually disappears, and only rutile phase seems to be left. However, the new phase is found to form by further enlargement and comparison with the profile of S5 (inset

of Figure 1). The three main peaks of S6 can be decomposed into two series, the peaks at 35.70°, 40.83°, 53.65° as well as 27.20° are attributed to rutile, and these at 35.84°, 41.01°, 54.06° cannot be designated to any one of known phases (here denoted as unidentified phase, UP), which suggests excessive Fe doping causes serious lattice distortion of some rutile due to the smaller ionic radius of Fe^{3+} (0.64 Å) than that of Ti^{4+} (0.68 Å) [45].

When Ti element was not involved in the reaction, the final product (S7) was identified to single phase of akaganeite according to the reference [46]. The XRD peaks do not overlap with these of other phases in S0–S6, which indicates iron substitutionally exists in lattice again.

For anatase in S0–S4, the relative ratio of the (004) peak intensity to that of the (101) peak, $I_{(004)}$:$I_{(101)}$ gradually increases from 0.218 to 0.337 (Table 1), which is larger than that of the standard pattern (0.20) and may be caused by more fluoride anions from FeF_3 with the function of morphology control, suggesting the oriented growth of sample along the (001) facet and a more thin thickness in the [001] direction [47,48], that is consistent with the following morphology results. However, the $I_{(004)}$:$I_{(101)}$ of anatase in S5 decreases to 0.245, which may be caused by new growth rates in some crystallographic directions due to the energy change of relevant facets arising from excessive Fe doping. It is noted when no doping, the increase of {001} facets suggests the enhancement of photocatalytic performance, which has been confirmed by previous studies [49]. However, for the Fe doped samples, the performance change is not consistent with this trend, because the negative effect caused by Fe-induced recombination of carriers must be also considered in addition to the effect of the active facets, which will be further investigated in the following sections.

Table 1. Relative ratio of the (004) peak intensity to that of the (101) peak for anatase in S0–S5 samples.

Sample	$I_{(004)}$:$I_{(101)}$	Sample	$I_{(004)}$:$I_{(101)}$
S0	0.218	S3	0.312
S1	0.252	S4	0.337
S2	0.267	S5	0.245

3.2. Morphology

The morphology of samples with different Fe contents is shown in Figure 2. For pure anatase TiO_2, most particles are single crystal and exhibit the truncated octahedral bipyramids which agree well with the results of references [16,39] and thus the two square surfaces can be safely concluded to the {001} facets and the eight isosceles trapezoidal surfaces to the {101} facets of anatase TiO_2 as indicated in Figure 2a.

After Fe doping, the morphology of anatase sample changes obviously. It can be seen from Figure 2b, even the lowest Fe content of S1 has promoted all single crystals to embed mutually and then form microspheres with the diameter of about 2–3 μm. The crystals composing microspheres look thinner than dispersive single crystals in Figure 2a, which indicates more fluoride anions from FeF_3 participate in the hydrolysis reaction as a capping agent, and could play a positive role in the enhancement of photocatalytic performance [41].

When the Fe content is not higher than that in S4, samples present the microsphere morphology consisted of bipyramids (Figure 2b,e), which indicates relatively small amount of Fe doping does not change the aggregation behavior of single crystals. However, it is noted that the thickness of single crystals decreases with the increase of fluoride anions, which indicates more {001} facets are produced with the increase of fluoride anions and agrees well with the order of $I_{(004)}$:$I_{(101)}$ in XRD results. In addition, there are some thick crystals in each product that may be caused by the local segregation of reactive ions.

When Fe content increases to 17.46%, the microspheres become to be composed of larger polyhedral crystals and smaller petal-shaped crystals (Figure 2f); when Fe content increases to 20.13%, the microspheres are composed of petal-shaped crystals similar to these in Figure 2f and dispersed dot crystals (Figure 2g). Combined with the results of XRD, the shared phase in S5 and S6 is drawn to rutile and hence bipyramid crystals are anatase and petal-shaped crystals are rutile for S5, petal-shaped crystals are rutile and dot crystals are unidentified phase for S6. Noted that in S5, anatase exhibits polyhedral shape with larger size which can be attributed to the new growth rate along different crystallographic directions and is consistent with the above XRD results. And for the same reason, the additional {110} facets are observed in the corners of the single crystals for S4 according to the references [50], as indicated in Figure 2e.

A noteworthy fact is that when with no Fe doping, most particles showed as single crystals and only a small part of them aggregated to microspheres, however after Fe doping, almost all particles embedded into microspheres. This phenomenon may be attributed to an increase in surface defects introduced by Fe doping. These defects raise the surface energy relative to pure anatase, thereby promoting the aggregation of doped particles to achieve greater thermodynamic stability.

For pure akaganeite sample (S7, Figure 2h), it clearly shows the prismatic form which can be aptly called as cigar-shape crystal which is consistent with other researches [51,52]. This crystal cannot be found in S1–S6, which indicates Fe ions do not form separate compound and further confirms Fe exists in the form of doping when the Fe contents is less than that in S6. Furthermore, the single crystals obtained here have the width of 2–3 μm and the length of greater than 10 μm, which make them more suitable as the model crystal to determine the structure of akaganeite than natural and previously synthetic akaganeite, because both of them typically occur as fine-grained masses and it is quite difficult to find suitable single crystal for diffraction studies [46].

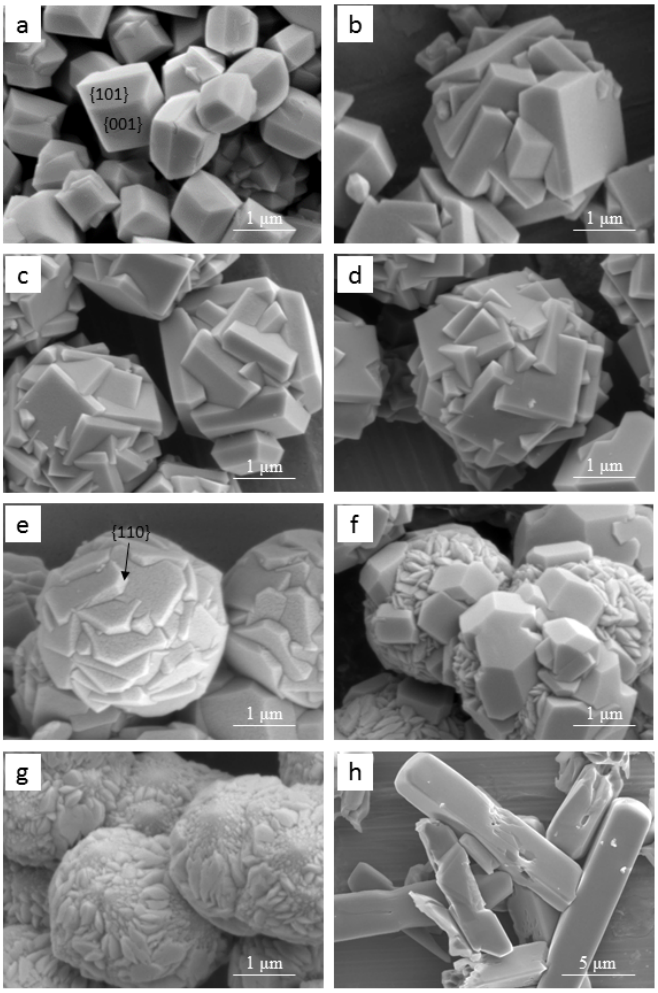

Figure 2. SEM images of pure TiO_2 sample S0 (**a**), Fe-doped samples S1–S6 (**b**–**g**) and akaganeite sample S7 (**h**).

3.3. XPS Analysis

To investigate the surface chemical states and elemental interactions within the synthesized materials, XPS characterization was performed (Figures 3–5). The high-resolution spectra of the undoped TiO_2 (S0), the Fe-doped TiO_2 series (S1–S6), and the goethite reference (S7) were analyzed. All Fe-doped samples (S1–S6) exhibited similar spectral features, indicating a consistent doping mechanism across the series. To illustrate the detailed chemical environment, the spectra for a representative sample, S2, were deconvoluted (Figure 4d–f).

The Ti 2p spectrum (Figure 4d) consists of a single spin-orbit doublet with characteristic peaks for Ti $2p_{3/2}$ and Ti $2p_{1/2}$ at 457.9 eV and 463.6 eV, respectively, confirming the +4 oxidation state of titanium. The Fe 2p spectrum (Figure 4e) displays a primary doublet for Fe $2p_{3/2}$ (710.7 eV) and Fe $2p_{1/2}$ (724.3 eV), accompanied by corresponding satellite peaks. The position of the Fe $2p_{3/2}$ peak confirms that iron is present in the +3 oxidation state. The O 1s spectrum (Figure 4f) is the most complex and informative. It can be resolved into four distinct components: the main peak at 530.1 eV corresponding to lattice oxygen in Ti-O-Ti bonds, a shoulder peak at 530.4 eV assigned to oxygen in newly formed Fe-O-Ti linkages, and two broader peaks at higher binding energies attributed to surface-adsorbed hydroxyl groups/water (-OH/H_2O) at 532.0 eV and adsorbed molecular oxygen or carbonates (O_2/CO_3^{2-}) at 533.0 eV [53–55].

Regarding the elemental spectra trends across all samples, the binding energy of the Ti 2p peaks shifts systematically with the iron content (Figure 3a). For the pure anatase sample (S0), the Ti $2p_{3/2}$ and Ti $2p_{1/2}$ peaks are located at 457.83 eV and 463.53 eV. At low doping levels (S1), these peaks exhibit a positive shift to higher binding energies. This shift suggests that electron density is withdrawn from the Ti^{4+} ions, which can be attributed to the formation of Ti-O-Fe linkages, given the higher electronegativity of Fe (1.8) compared to Ti (1.5) [56]. This confirms that Fe and Ti are mixed at an atomic level, consistent with the XRD results. However, as the doping concentration further increases (S2–S6), the Ti 2p peaks exhibit a continuous negative shift back towards lower binding energies. This reversal is likely caused by the formation of oxygen vacancies (V_0) to maintain charge neutrality when substituting Ti^{4+} with Fe^{3+}. These vacancies act as electron-donating centers, increasing the electron density around the neighboring Ti^{4+} ions and thus lowering their binding energy [57,58].

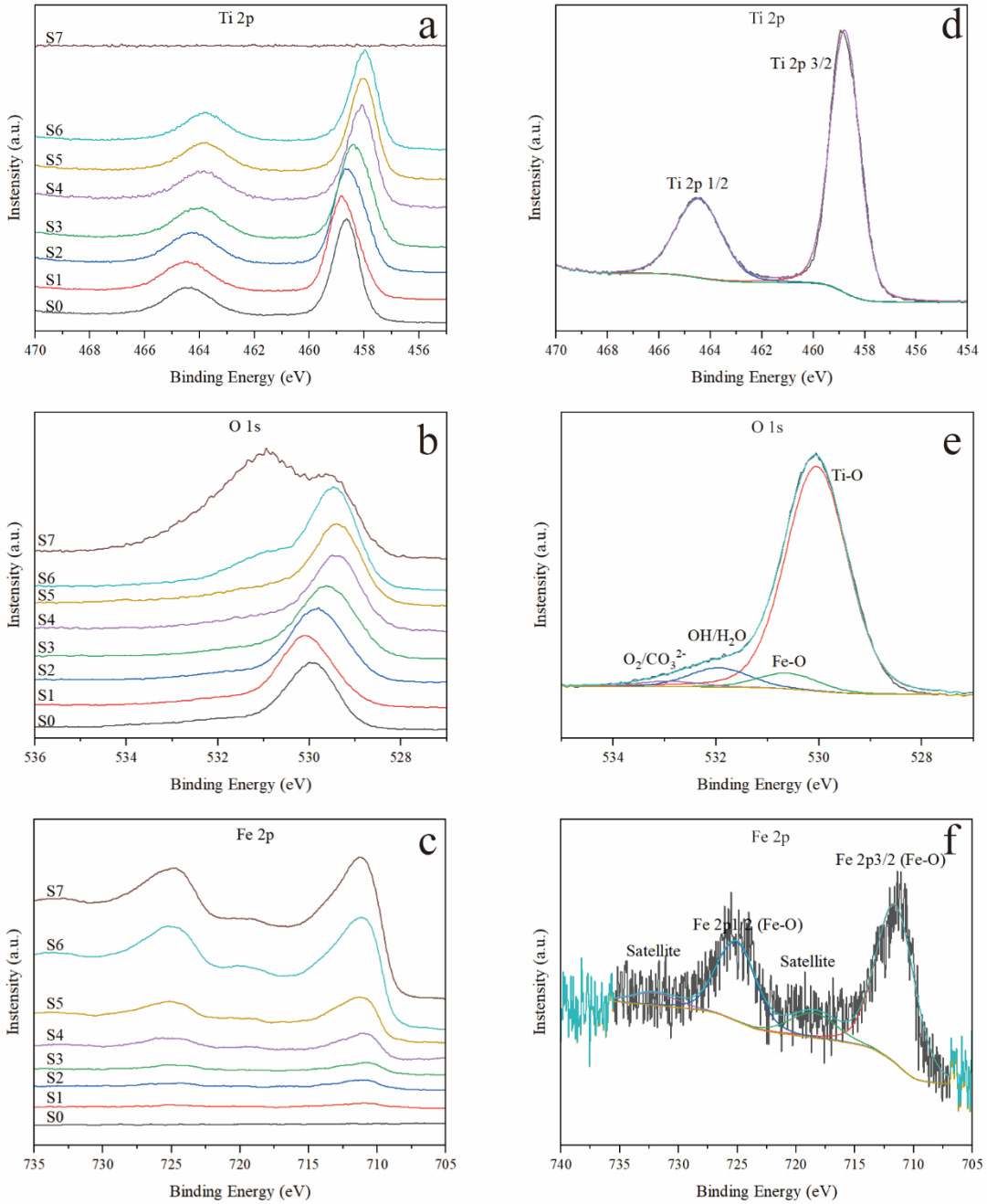

Figure 3. Comparison of the XPS peaks for Ti 2p (**a**), O 1s (**b**), and Fe 2p (**c**) across different samples; and peak deconvolution of the XPS spectra for Ti 2p (**d**), O 1s (**e**), and Fe 2p (**f**) of sample S2.

The trend of the main O 1s peak from lattice Ti-O mirrors that of the Ti 2p peaks, first shifting positively and then negatively with increasing Fe content (Figure 4). The initial positive shift relative to pure anatase (S0) further affirms the formation of Fe-O-Ti atomic linkages, as the binding energy of oxygen in this environment lies between that of pure Ti-O-Ti and pure Fe-O-Fe bonds. As the Fe content increases, the subsequent negative shift toward

the binding energy of S6 can also be attributed to the increasing concentration of oxygen vacancies, which donate electron density to the lattice oxygen atoms. Notably, the characteristic peaks for lattice oxygen in pure akaganeite or α-Fe_2O_3 were not observed in any of the doped samples, confirming that no separate iron oxide phases were formed [24].

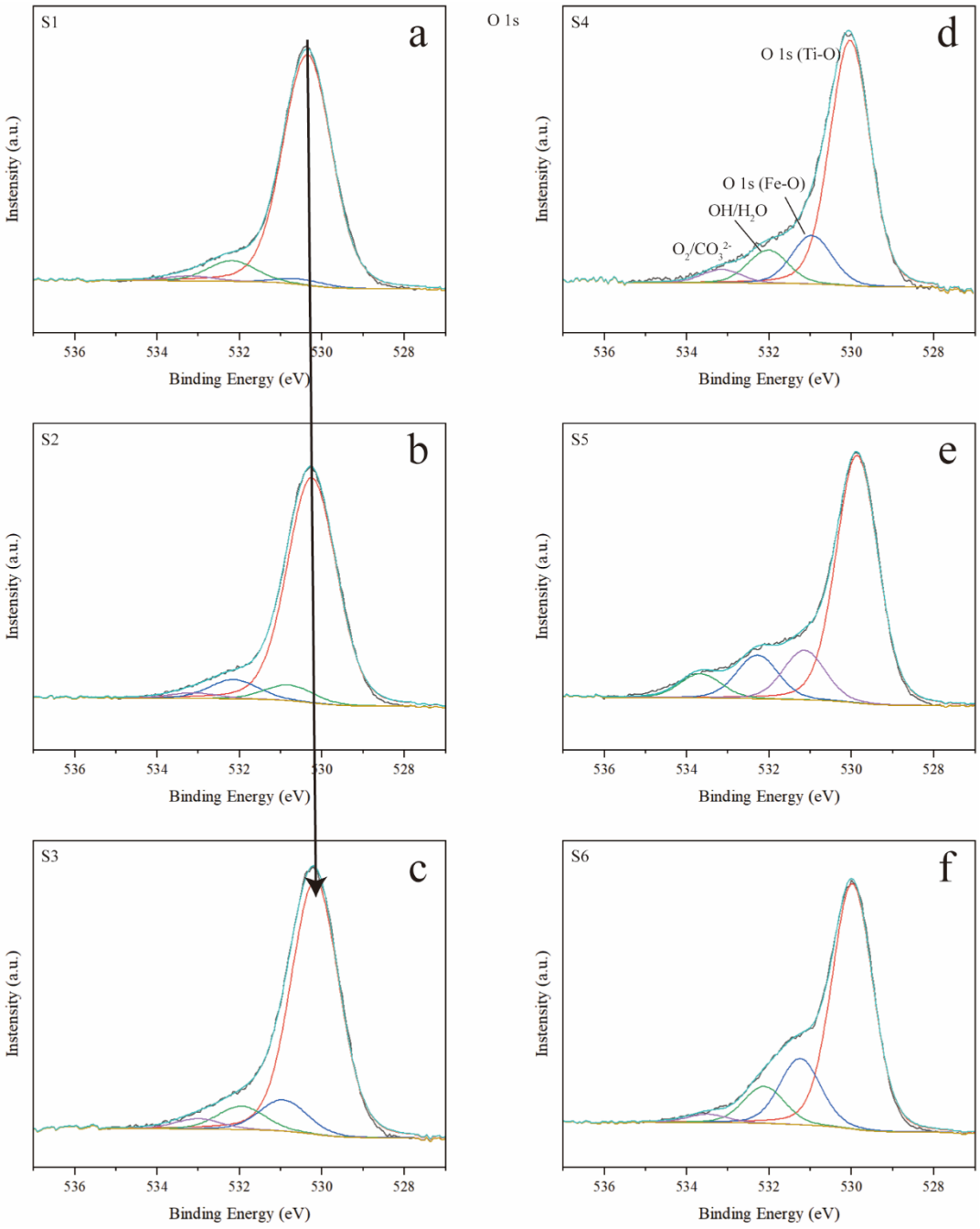

Figure 4. The high-resolution O1s spectra of S1–S6 (**a**–**f**) samples with deconvoluted components.

For the pure TiO_2 sample S1, there is no contribution of Fe-O in the O1s peak (Figure 5a); while for the goethite sample S7, 529.82 eV peak corresponds to the oxygen in Fe-O, 531.11 eV corresponds to the oxygen in Fe-OH, 532.09 and 533.08 eV correspond to the oxygen in surface-adsorbed hydroxyl groups/water (-OH/H_2O) and adsorbed molecular oxygen or carbonates (O_2/CO_3^{2-}), respectively (Figure 5b) [53–55].

Furthermore, the deconvoluted O 1s spectra allow for a quantitative estimation of the actual incorporated iron content. By calculating the ratio of the integrated peak areas, Fe-O/(Fe-O + Ti-O), the atomic fractions of Fe in samples S1–S6 were estimated to be 2.36%, 6.58%, 10.99%, 16.53%, 17.98%, and 21.29% (Table 2), respectively, which are very close to the results of ICP-OES. This result clearly indicates that not all iron from the FeF_3 precursor was incorporated into the TiO_2 lattice.

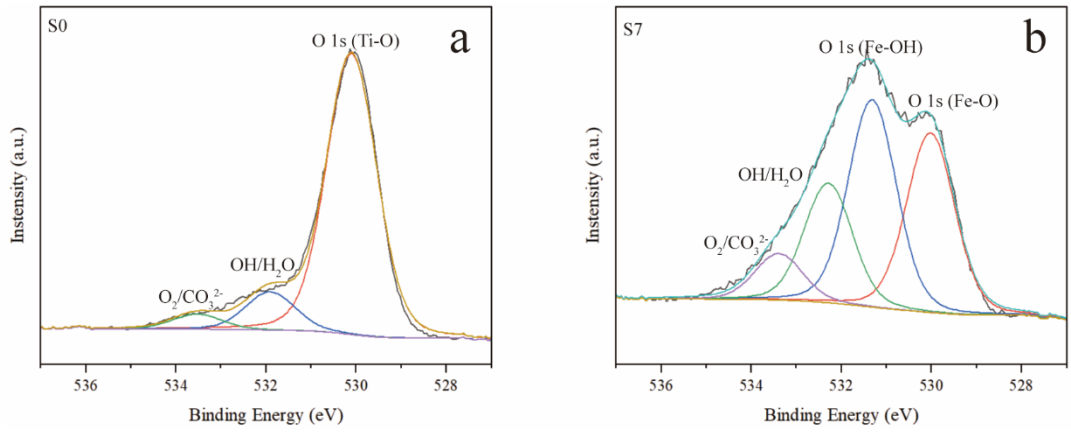

Figure 5. The high-resolution O1s spectra of S0 (**a**) and S7 (**b**) with deconvoluted components.

No Fe 2p signal was detected for the undoped S0 sample. For the doped samples, the Fe $2p_{3/2}$ peak position shifts progressively to higher binding energies with increasing dopant concentration, moving from 710.55 eV in S1 towards the 711.35 eV observed in the goethite reference S7 (Figure 4c). This positive shift can be attributed to changes in the local coordination environment around the Fe^{3+} ions. At higher concentrations, Fe^{3+} ions tend to aggregate, causing local structural deformation. This formation of iron-rich domains, coupled with the proximity to charge-compensating oxygen vacancies, can attract hydroxyl groups or water molecules, creating a local structure that increasingly resembles that of FeOOH. This change in the chemical environment around the iron atoms results in the observed progressive shift to higher binding energies [59–62].

Table 2. Peak fitting information of O1s in Fe-doped TiO_2 samples.

Samples	Ti-O	Fe-O	OH/H_2O	O_2/CO_3^{2-}	Fe-O/(Fe-O + Ti-O)
	Peak Position (eV), and AREA Percentage (%)				
S1	530.1 88.1%	530.4 2.13%	532.0 7.90%	533.0 1.87%	2.36%
S2	530.0 84.65%	530.6 5.96%	531.9 7.29%	532.9 2.10%	6.58%
S3	529.9 79.54%	530.7 9.82%	531.7 7.37%	532.8 3.27%	10.99%
S4	529.7 71.93%	530.7 14.24%	531.8 9.79%	533.0 4.04%	16.53%
S5	529.7 66.71%	530.9 14.62%	532.1 12.00%	533.4 6.68%	17.98%
S6	529.8 68.68%	531.0 18.58%	531.9 10.38%	533.3 2.36%	21.29%

3.4. UV-DRS Analysis

It is known that chemical doping with transition metal ions can alter the semiconductor properties of a TiO_2 matrix [63,64] So, the UV-vis diffuse reflectance spectra of as prepared samples were further characterized and then normalized as shown in Figure 6a. Further calculations of the DRS curves yielded Tauc plots of the $(\alpha hv)^{1/2}$ versus hv, where α is the absorption coefficient, h is the Planck constant, and v is the incident light frequency (Figure 6b). Extrapolating the straight lines revealed band gaps of 2.85, 2.27, 2.24, 2.18, 2.10, 1.82, 1.83, and 1.83 eV for samples S0–S7, respectively. The band gap of S0 is lower than the typical 3.2 eV, likely due to the surface fluorine atoms and oxygen vacancies inducing surface atomic rearrangement to form surface defect states or impurity energy levels. The band gap decreases with increasing Fe doping, reflecting the significant effect of Fe doping on the light absorption capacity of the samples. Pure anatase sample (S0) exhibits a broad band in the short wavelength region of less than 400 nm corresponding to the intrinsic absorption. In comparison, S1 with low Fe content shows an obvious red shift and a new adsorption peak in 450–500 nm region responding to the excitation of 3d electrons of Fe^{3+} ion into the conduction band of TiO_2, which is in agreement with the previous reports [65]. With increase of Fe content, the maximal absorption peak is shifted towards visible light region, at the same time the intensity of new absorption peak increases gradually, once again this phenomenon indicates irons are doped substitutionally for Ti ions. When Fe content reaches that in S5, the movement of the absorption peak is more

significant, and the peak at low energy position becomes stronger than that at high energy position, corresponding to the phase change owing to excessive Fe doping. From S6 to S7, the similar change with S5 continues to take place. The enhanced absorption in the visible-light region may be attributed to the charge transfer transition between iron ions ($Fe^{3+} + Fe^{3+} \rightarrow Fe^{4+} + Fe^{2+}$) at about 440–550 nm [66], thus this result also indicates iron ions form considerable local aggregation in TiO_2 matrix which is consistent with the above XPS measurements. Moreover, noted that the DRS only represents the absorption capacity of samples to each wavelength of UV-vis light, while photocatalytic performance also depends on the recombination of photogenerated carriers, which requires other means for further characterization, for example, the following PL measurements.

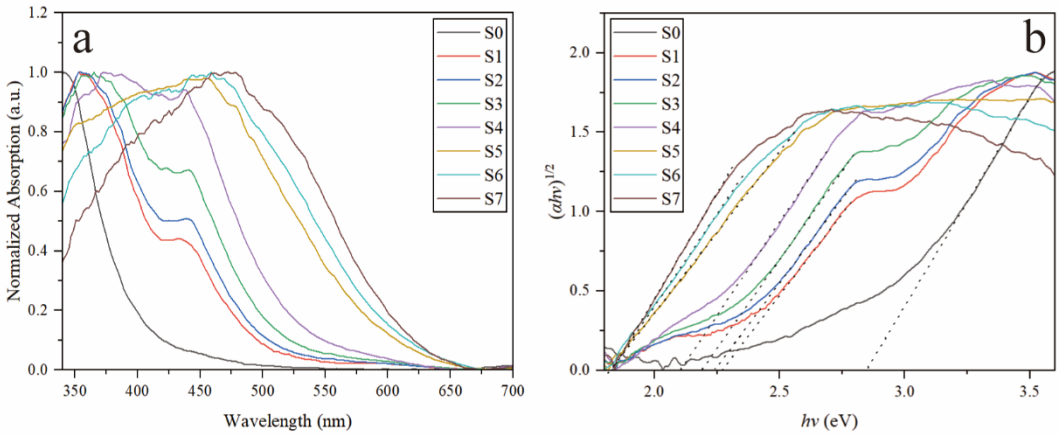

Figure 6. UV-vis diffuse reflectance absorption spectra (**a**), and Tauc plots of the $(ahv)^{1/2}$ versus hv (**b**) of samples.

3.5. PL Patterns

PL emission results from the recombination of free carriers and has been widely used to investigate the efficiency of charge trapping, immigration, transfer and to understand the fate of electron-hole pairs in semiconductor. The intensity and wavelength of PL spectra are sensitive to the doping of aliovalent ions [67]. Figure 7 shows comparison of PL spectra of pure anatase and Fe doped samples with different Fe contents. All the spectra have the similar shape and a main peak appears at 488 nm which is equivalent to 2.54 eV and can be ascribed to bound excitons [68]. Figure 7 gives the intensity order of S7 > S4 > S6 > S5 > S3 > S0 > S2 > S1, which reveals the lower recombination rate of electron–hole pairs and hence higher separation efficiency for S1 and S2 with low Fe contents, resulting in the enhancement of photocatalytic activity because more photogenerated charge carriers can participate in the photochemical transformation [68]. When the Fe concentration is excessive (S3–S7), the PL intensities are stronger than that of S0. This can be explained by the dual role of Fe^{3+} ions: at low concentrations, they mainly act as charge-trapping sites that promote electron-hole separation; however, at higher concentrations, they become recombination centers.

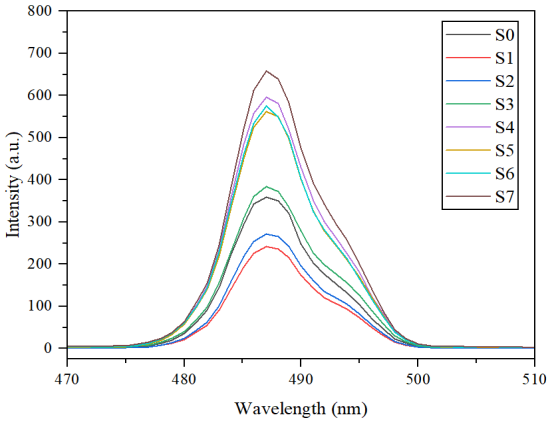

Figure 7. PL spectra of samples.

For anatase, it is well known that the increase of {001} facets can enhance the photocatalytic activity of samples [16,40,49], however the PL results here are just the opposite, which indicates the negative effects caused

by Fe doping may gradually surpass the positive effects caused by the increase of active facets. It is conceivable when the Fe content is at a certain value, for example, 2.3% or less, active facets and doping can function together, leading to the optimal photocatalytic effect, which can be further studied by trying more doping amount with FeF_3 as iron dopant in the future work.

3.6. Photocatalytic Performance

The photocatalytic activity of the samples was investigated by detection of •OH which are considered as the most important oxidative species [69]. TA was used as a fluorescence probe because it can react with •OH in basic solution to generate 2-hydroxy terephthalic acid (TAOH), which emits unique fluorescence signal with the spectrum peak around 426 nm [70]. Figure 8a shows the changes in the PL spectra of TA solution under UV light with increasing irradiation time for a typical sample, S1. A gradual increase in the PL intensity at 426 nm is observed with increasing time. This indicates that PL arises from luminescent TAOH produced by chemical reaction between TA and •OH formed during photocatalytic process. The production of •OH under light radiation follow a pseudo-zero-order reaction rate equation in kinetics for all samples (Figure 8b). The linear relationship between fluorescence intensity and irradiation time indicates that the photocatalytic reaction follows pseudo-zero-order kinetics under these conditions [71]. The rate constants for S1–S6 are 0.480 min^{-1}, 0.431 min^{-1}, 0.336 min^{-1}, 0.292 min^{-1}, 0.314 min^{-1} and 0.310 min^{-1} respectively. For comparison, the rate constants for pure anatase and akaganeite are 0.378 min^{-1} and 0.283 min^{-1}. It can be seen that the doped TiO_2 samples with low Fe content, S1 and S2, show enhanced photocatalytic activity compared to pure anatase, but when Fe content continues to increase, the photocatalytic activity decreases, which confirms the PL results in Figure 7 and can be attributed to the dual role of dopant discussed in the following.

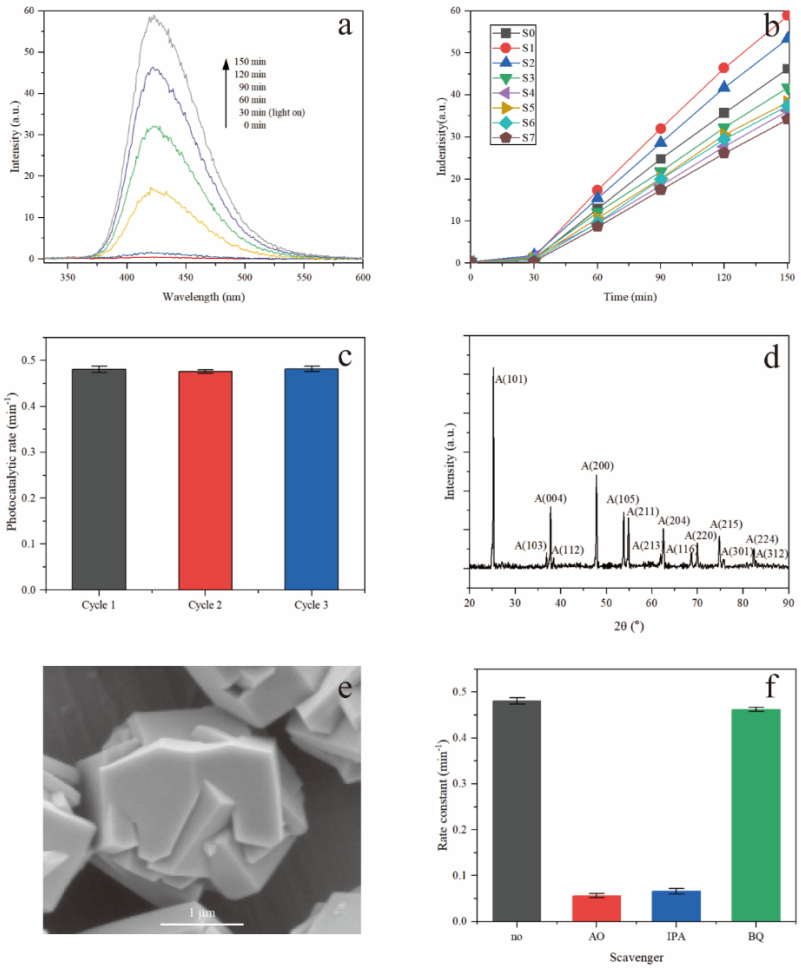

Figure 8. PL spectral evolution with irradiation time for representative S1 (**a**), the relationship between fluorescence intensity at 426 nm and irradiation time of various samples (**b**). Cycle tests (**c**), XRD pattern (**d**) and SEM image (**e**) after cycle tests, and active species trapping experiments (**f**) for S1.

Three consecutive photocatalytic cycling tests were performed and the results show no significant decrease in performance for S1, indicating high reusability and stability (Figure 8c). The sample after the cycling tests were characterized using XRD and SEM and (Figure 8d,e). The obtained XRD pattern confirms that the sample remains in the pure anatase phase with no changes to its crystal structure. Furthermore, the morphology was well-maintained, still exhibiting the structure of microspheres assembled from truncated octahedra, with no obvious fragmentation. In addition, to check for potential iron leaching, the used catalyst was also analyzed with ICP-OES. The measured Fe fraction was 2.20%, which is nearly identical to the content in the as-prepared sample (2.23%). This confirms that no significant iron leaching occurred during the photocatalytic process.

A series of active species trapping experiments were conducted and the results confirmed that hydroxyl radicals (•OH) and holes (h^+) are the primary active species responsible for the photocatalytic process, while superoxide radicals (O_2^-) are not a major contributor (Figure 8f). This finding further corroborates the original photocatalytic results. Furthermore, the minor role of superoxide radicals can be explained by the electronic structure of the Fe-doped TiO_2. The introduction of iron creates Fe 3d impurity energy levels within the band gap of TiO_2. These levels not only narrow the band gap but also act as effective trapping sites for photo-excited electrons, causing the reduction of Fe^{3+} to Fe^{2+}. This process efficiently captures electrons, preventing them from reacting with adsorbed oxygen to form superoxide radicals. Only a small number of electrons might undergo a secondary transition from these impurity levels to the intrinsic conduction band, leading to a significantly lower yield of superoxide ions [41].

3.7. The Dual Role of Dopant in Photocatalytic Performance

The dual role of dopant in photocatalytic performance can be schematically illustrated in Figure 9, including morphology control (Role 1) and doping (Role 2). Here, Fe doped samples are divided into two categories for more convenient discussion according to the detail difference of the Role 1 and 2 of samples, while undoped anatase and akaganeite are discussed separately as the comparison.

Category 1 is the samples with single phase of anatase, that is, S1–S4, in which F ions from dopant play an important role of morphology control. The F^- present in the system act as a highly efficient capping agent, preferentially adsorbing onto the high-energy {001} facets of the anatase crystals. This selective adsorption stabilizes the {001} facets, inhibiting their growth and promoting anisotropic crystal development. Consequently, as the FeF_3 concentration increases, the crystal morphology evolves from relatively thick truncated octahedra to thin nanoplates with a significantly higher specific surface area. This morphological optimization provides two key catalytic advantages: first, it drastically increases the exposure of the highly reactive {001} facets, furnishing more active sites for reactant adsorption and catalysis [72]. Second, the thin structure substantially shortens the diffusion path for photo-generated charge carriers to travel from the bulk to the surface, effectively suppressing the probability of bulk recombination.

The second facet of this dual role for category 1 lies in the modulation of the electronic structure. When Fe^{3+} ions are substitutionally incorporated into the TiO_2 lattice, they effectively engineer the semiconductor's band structure. The introduction of Fe 3d orbitals creates impurity energy levels within the TiO_2 band gap [73]. These levels reduce the energy required for electron excitation, causing a red-shift in the material's absorption edge and enabling the harvesting of lower-energy visible-light photons, thereby improving the overall light utilization efficiency. Furthermore, at these moderate concentrations, the Fe^{3+} sites serve as efficient trapping centers for photo-generated electrons. This process spatially separates the electrons and holes, inhibiting their rapid recombination. The resulting enhancement in charge separation efficiency significantly prolongs the lifetime of charge carriers, which in turn boosts the quantum yield for the generation of reactive oxygen species, such as hydroxyl radicals (•OH).

For more details about Fe^{3+} can act as electron and hole shallow traps, the oxidation level (Fe^{3+}/Fe^{4+}) may fall above the valence band top of TiO_2 and the reduction level (Fe^{3+}/Fe^{2+}) may be under the conduction band bottom of TiO_2 [74–76]. Fe^{2+} can be formed by means of a transfer of photogenerated electrons from TiO_2 to Fe^{3+} following Equation (1), however Fe^{2+} is relatively unstable due to the loss of d5 electronic configuration, and tends to return to Fe^{3+} according to the crystal field theory. As a result, Fe^{2+} could be oxidized to Fe^{3+} by transferring electrons to absorbed O_2 on the surface of TiO_2 (Equation (2)) [77]. Meanwhile, photogenerated holes can transfer from the valence band of TiO_2 to oxidize Fe^{3+} to Fe^{4+} due to the potential difference between the valence band top of TiO_2 and the oxidation level (Fe^{3+}/Fe^{4+}) (Equation (3)). Then, following Equation (4), the trapped holes in Fe^{4+} can migrate to the surface adsorbed hydroxy ion to produce hydroxyl radical [78].

$$Fe^{3+} + e^- \rightarrow Fe^{2+} \quad (1)$$

$$Fe^{2+} + O_2 \rightarrow Fe^{3+} + O_2\bullet^- \quad (2)$$

$$Fe^{3+} + h^+ \rightarrow Fe^{4+} \quad (3)$$

$$Fe^{4+} + OH^- \rightarrow Fe^{2+} + OH\bullet \quad (4)$$

In this regime, the morphological and electronic effects are synergistic. The morphological engineering provides a superior physical platform for the catalytic reaction, while the electronic modulation enhances the efficiency with which this platform generates active species. This interplay between an optimized morphology and enhanced electronic properties leads to the marked increase in photocatalytic activity. It is important to note, however, that this synergistic enhancement has an optimal threshold, beyond which the Fe^{3+} sites increasingly act as recombination centers, leading to an eventual inhibition of the catalytic activity.

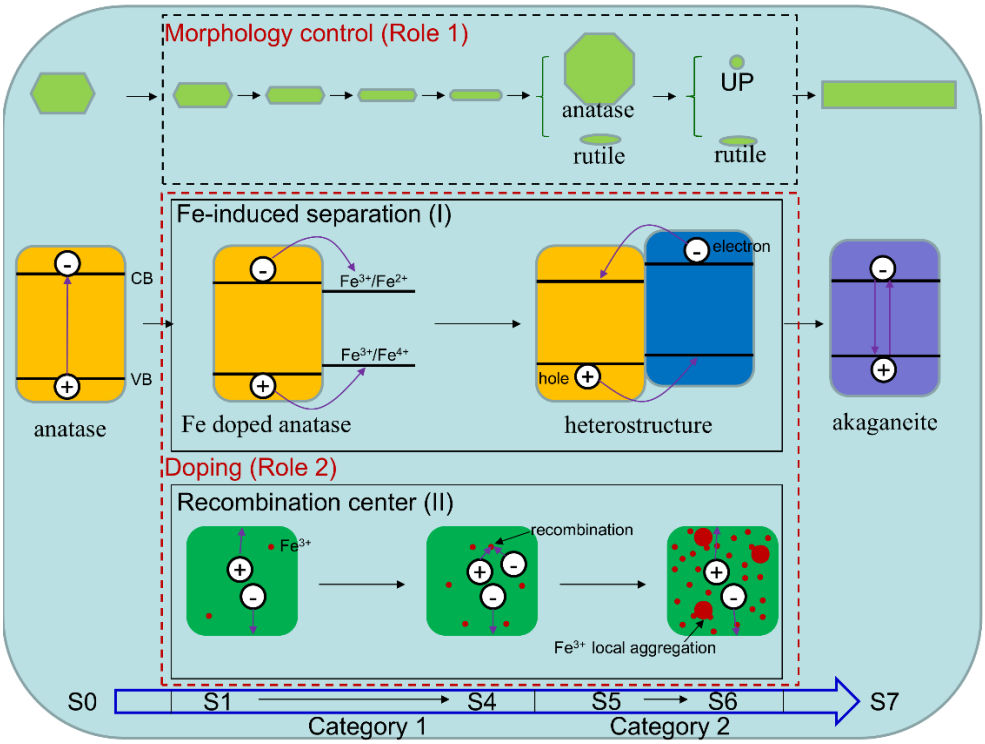

Figure 9. Dual role of dopant in enhancing photocatalytic performance.

More specifically, Fe^{3+} ions act as recombination centers following the Equations (5) and (6). After the formation from Fe^{3+}, Fe^{2+} could be also reduced to Fe^{3+} by absorbing photogenerated holes. These reactions are in competition with the redox processes that can occur at the solid–liquid interface (Equations (1)–(4)), thus an optimum amount of iron doping must exist working with the best photocatalytic efficiency.

$$Fe^{3+} + e^- \rightarrow Fe^{2+} \quad (5)$$

$$Fe^{2+} + h^+ \rightarrow Fe^{3+} \quad (6)$$

When the amount of dopant is small, morphology control and Fe-induced separation dominate the photocatalytic process, the recombination of photogenerated charge carriers is inhibited to enhance their lifetime, thus photocatalytic performance is improved, for example S1. With the increase of dopant, the effect of carrier recombination increases gradually, therefore photocatalytic performance begins to decrease at a certain doping amount, for example S2. When the amount of Fe^{3+} is high, the recombination becomes to be dominant, this means photogenerated carriers do not have enough time to transfer to the surface [77] to form active species with other molecules or groups because of too many obstacles on the path of movement. As a result, photocatalytic performance gradually decreases, for example S3 and S4.

Category 2 is the biphasic samples, that is, S5 and S6. In the formation process of S5, although there are more fluoride ions as shape control agent, the content of iron ions is also relatively high, which may cause the energy change of facets and thus anatase sheets do not become thinner than these in S4. In the case of such a highly doped, evaluation of the activity level and contribution to photocatalytic performance of each facet is rather difficult.

However, rutile, another phase in S5 with petal-shaped morphology, can possess large surface and thus promote the enhancement of photocatalytic efficiency, as well as other photocatalysts with similar appearance [79]. In S6, the rutile phase inherits this advantage, at the same time another phase with dot particles may also has the similar characteristic, both of which thus play an active role in determining the performance of sample. On the other hand, iron doping will simultaneously change the band structure and position of the constituent phases, and may even form a suitable heterojunction [80–86]. as well as the manner in other systems [87–90], contributing to the enhancement of photocatalytic performance, more or less. After all, the two end members of Fe doping TiO_2, anatase and akaganeite are common photocatalytic semiconductor with suitable bandgap between about 1.8–3.2 eV [91]. In the meantime, more and more serious recombination is caused by the increasingly iron doping in the aforementioned way, which can compete with the effects of surface area and heterostructure, leading to the performance diversity among S5, S6 and S4.

For pure anatase (S0), a considerable number of {001} facets are exposed, however the visible portion of the spectrum can be not utilized effectively due to the larger bandgap, and only a few photogenerated electrons and holes are produced by intrinsic excitation, so S0 does not show the highest photocatalytic performance. For pure akaganeite, the band gap of 1.83 eV is suitable for electronic transitions from valence band to conduction band [92,93], thus it can also exhibit some photocatalytic activity which has been confirmed by other researchers [94,95]. However, photogenerated carriers can easily recombine by self-relaxation in the similar way with other narrow bandgap compounds [96,97], so S7 shows the lowest photocatalytic performance.

4. Conclusions

In summary, by choosing FeF_3 as iron source, Fe doped anatase microspheres composed of embedded single crystals with exposed {001} facets have been synthesized successfully. The sample (S1) with the best photocatalytic performance in the range of the study has the Fe content of about 2.23%. Moreover, the effect of different amounts of dopant on structure, morphology, optical property and photoactivity were investigated. XRD and SEM results indicate that with the increase of Fe doping, successive phase transitions appear gradually. When at low doping, S1–S4 have the single phase of anatase, in which anatase sheets become thinner and thinner; when at high doping, S5 has the mixed phases of bipyramid anatase and petal-shaped rutile, S6 has the mixed phases of petal-shaped rutile and dot UP. XPS results confirm Fe ions are doped substitutionally for Ti ions. DRS results reveal the gradual red shift with the increase of Fe content. PL results is consistent with photocatalytic test results, which shows the photocatalytic efficiency of samples are controlled by the synergetic effect of morphology, Fe induced separation and recombination of photogeneration carriers, and thus the dual role of dopant was discussed in detail. Our study not only provides a novel approach to dope TiO_2 for better commodity, but also affords experience of the precise adjustment of morphology, performance for other photocatalysts.

Author Contributions

J.W.: Formal Analysis, Writing—Original Draft. J.N.: Conceptualization, Methodology, Supervision, Writing—review & editing. J.B.: Formal Analysis, Visualization. L.H.: Formal Analysis, Visualization. D.W.: Formal Analysis, Visualization. Y.L.: Formal Analysis, Visualization. P.F.: Resources, Funding acquisition, Project administration. All authors have read and agreed to the published version of the manuscript.

Funding

This work is supported by the Undergraduate Innovation Training Program of Jangsu Province (S202510290270), the China University of Mining and Technology (CUMT) Open Sharing Fund for Large-scale Instruments and Equipment (DYGX-2025-63), and the National Natural Science Foundation of China (Grant Nos. 52020105011).

Institutional Review Board Statement

Not applicable.

Informed Consent Statement

Not applicable.

Data Availability Statement

The data that has been used is confidential.

Conflicts of Interest

The authors declare no conflict of interest. The funders had no role in the design of the study; in the collection, analyses, or interpretation of data; in the writing of the manuscript; or in the decision to publish the results.

References

1. Liu, G.; Yang, H.G.; Pan, J.; et al. Titanium dioxide crystals with tailored facets. *Chem. Rev.* **2014**, *114*, 9559.
2. Grätzel, M. Dye-sensitized solar cells. J. *Photoch. Photobio. C* **2003**, *4*, 145.
3. Kubacka, A.; Fernández-García, M.; Colón, G. Advanced nanoarchitectures for solar photocatalytic applications. *Chem. Rev.* **2011**, *112*, 1555.
4. Niu, J.N.; Shen, S.S.; He, S.F.; et al. Synthesis and photoactivity of anatase porous single crystals with different pore sizes. *Ceram. Int.* **2015**, *41*, 11936.
5. Zhou, W.; Du, G.; Hu, P.; et al. Nanoheterostructures on TiO_2 nanobelts achieved by acid hydrothermal method with enhanced photocatalytic and gas sensitive performance. *J. Mater. Chem.* **2011**, *21*, 7937.
6. Zhu, W.D.; Wang, C.W.; Chen, J.B.; et al. Enhanced field emission from hydrogenated TiO_2 nanotube arrays. *Nanotechnology* **2012**, *23*, 455204.
7. Fujishima, A.; Honda, K. Electrochemical photolysis of water at a semiconductor electrode. *Nature* **1972**, *238*, 37.
8. Tong, H.; Ouyang, S.; Bi, Y.; et al. Nano-photocatalytic materials: possibilities and challenges. *Adv. Mater.* **2012**, *24*, 229.
9. Chen, R.Y.; Lai, D.X.; Wang, D.X.; et al. Enhanced photocatalytic activity of kaolinite-TiO_2-graphene oxide composite with a porous stacking structure. *J. Alloy Compd.* **2021**, 889, 161682.
10. Li, C.; Sun, L.; Niu, J.; et al. Core-shell Bi-containing spheres and TiO_2 nanoparticles co-loaded on kaolinite as an efficient photocatalyst for methyl orange degradation. *Catal. Commun.* **2023**, 175, 106609.
11. Li, C.; Shen, S.; Niu, J.; et al. Mesoporous single-crystal-based TiO_2 microspheres decorated by carbon nitride for obviously improved photocatalytic performance and recyclability. *Inorg. Chem. Commun.* **2023**, 150, 110524.
12. Liu, L.; Chen, X. Titanium dioxide nanomaterials: self-structural modifications. *Chem. Rev.* **2014**, *114*, 9890.
13. Chen, D.H.; Caruso, R.A. Recent progress in the synthesis of spherical titania nanostructures and their applications. *Adv. Funct. Mater.* **2013**, *23*, 1356.
14. Berger, H.; Tang, H.; Levy, F. Growth and Raman spectroscopic characterization of TiO_2 anatase single crystals. *J. Cryst. Growth.* **1993**, *130*, 108.
15. Niu, J.N.; Shen, S.S.; Zhou, L.; et al. Synthesis and hydrogenation of anatase TiO_2 microspheres composed of porous single crystals for significantly improved photocatalytic activity. *RSC Adv.* **2016**, *6*, 62907.
16. Yang, H.G.; Sun, C.H.; Qiao, S.Z.; et al. Anatase TiO_2 single crystals with a large percentage of reactive facets. *Nature* **2008**, *453*, 638.
17. Choi, W.; Termin, A.; Hoffmann, M.R. The role of metal ion dopants in quantum-sized TiO_2: Correlation between photoreactivity and charge carrier recombination dynamics. *J. Phys. Chem.* **1994**, *98*, 13669.
18. Litter, M.I. Heterogeneous photocatalysis: transition metal ions in photocatalytic systems. *Appl. Catal. B* **1999**, *23*, 89.
19. Shen, S.S.; Niu, J.N.; Shen, S.T.; et al. A method for adjusting nitrogen doping amount in anatase TiO_2 single crystals with well-faceted shape and micron size. *J. Phys. Chem. Solids* **2017**, *107*, 75.
20. Adán, C.; Bahamonde, A.; Fernández-García, M.; et al. Structure and activity of nanosized iron-doped anatase TiO_2 catalysts for phenol photocatalytic degradation. *Appl. Catal. B-Environ.* **2007**, *72*, 11.
21. Delekar, S.D.; Yadav, H.M.; Achary, S.N.; et al. Structural refinement and photocatalytic activity of Fe-doped anatase TiO_2 nanoparticles. *Appl. Surf. Sci.* **2012**, *263*, 536.
22. Reddy, J.K.; Lalitha, K.; Reddy, P.V.L.; et al. Fe/TiO_2: A Visible Light Active Photocatalyst for the Continuous Production of Hydrogen from Water Splitting Under Solar Irradiation. *Catal. Lett.* **2014**, *144*, 340.
23. Sun, T.; Liu, E.; Fan, J.; et al. High photocatalytic activity of hydrogen production from water over Fe doped and Ag deposited anatase TiO_2 catalyst synthesized by solvothermal method. *Chem. Eng. J.* **2013**, *228*, 896.
24. Abdulla-Al-Mamun, M.; Kusumoto, Y.; Islam, M.S. Enhanced photocatalytic cytotoxic activity of Ag@ Fe-doped TiO_2 nanocomposites against human epithelial carcinoma cells. *J. Mater. Chem.* **2012**, *22*, 5460.
25. Wang, S.; Lian, J.S.; Zheng, W.T.; et al. Photocatalytic property of Fe doped anatase and rutile TiO_2 nanocrystal particles prepared by sol–gel technique. *Appl. Surf. Sci.* **2012**, *263*, 260.
26. Kim, T.H.; Rodríguez-González, V.; Gyawali, G.; et al. Synthesis of solar light responsive Fe, N co-doped TiO_2 photocatalyst by sonochemical method. *Catal. Today* **2013**, *212*, 75.
27. Zhang, K.; Wang, X.; Guo, X.; et al. Release of engineered nanomaterials from personal care products throughout their life cycle. *J. Nanopart. Res.* **2014**, *16*, 1.

28. Feilizadeh, M.; Mul, G.; Vossoughi, M. E. coli inactivation by visible light irradiation using a Fe–Cd/TiO_2 photocatalyst: statistical analysis and optimization of operating parameters. *Appl. Catal. B-Environ.* **2015**, *168*, 441.
29. Larumbe, S.; Monge, M.; Gómez-Polo, C. Comparative study of (N, Fe) doped TiO_2 photocatalysts. *Appl. Surf. Sci.* **2015**, *327*, 490.
30. Kaur, N.; Shahi, S.K.; Singh, V. Synthesis, characterization and photocatalytic activity of magnetically separable γ-Fe_2O_3/N, Fe codoped TiO_2 heterojunction for degradation of Reactive Blue 4 dye. *RSC Adv.* **2015**, *5*, 61623.
31. Kuvarega, A.T.; Krause, R.W.; Mamba, B.B. Comparison between base metals and platinum group metals in nitrogen, M codoped TiO_2 (M= Fe, Cu, Pd, Os) for photocatalytic removal of an organic dye in water. *J. Nanomater.* **2014**, *2014*, 962102.
32. Zhang, Y.; Cheng, K.; Lv, F.; et al. Photocatalytic treatment of 2, 4, 6-trinitotoluene in red water by multi-doped TiO_2 with enhanced visible light photocatalytic activity. *Colloids Surf. A* **2014**, *452*, 103.
33. Chen, B.; Haring, A.J.; Beach, J.A.; et al. Visible light induced photocatalytic activity of Fe^{3+}/Ti^{3+} co-doped TiO_2 nanostructures. *RSC Adv.* **2014**, *4*, 18033.
34. Sun, T.; Liu, E.; Liang, X.; et al. Enhanced hydrogen evolution from water splitting using Fe-Ni codoped and Ag deposited anatase TiO_2 synthesized by solvothermal method. *Appl. Surf. Sci.* **2015**, *347*, 696.
35. Liu, T.; Zhang, H. Novel Fe-doped anatase TiO_2 nanosheet hierarchical spheres with 94%{001} facets for efficient visible light photodegradation of organic dye. *RSC Adv.* **2013**, *3*, 16255.
36. Yu, Y.; Cao, C.; Li, W.; et al. Low-cost synthesis of robust anatase polyhedral structures with a preponderance of exposed {001} facets for enhanced photoactivities. *Nano Res.* **2012**, *5*, 434.
37. Lazzeri, M.; Vittadini, A.; Selloni, A. Structure and energetics of stoichiometric TiO_2 anatase surfaces. *Phys. Rev. B* **2001**, *63*, 155409.
38. Lazzeri, M.; Vittadini, A.; Selloni, A. Erratum: Structure and energetics of stoichiometric TiO_2 anatase surfaces. *Phys. Rev. B* **2002**, *65*, 119901.
39. Li, H.; Zeng, Y.; Huang, T.; et al. Controlled synthesis of anatase TiO_2 single crystals with dominant {001} facets from TiO_2 powders. *ChemPlusChem* **2012**, *77*, 1017.
40. Yang, H.G.; Liu, G.; Qiao, S.Z.; et al. Solvothermal synthesis and photoreactivity of anatase TiO_2 nanosheets with dominant {001} facets. *J. Am. Chem. Soc.* **2009**, *131*, 4078.
41. Jo, W.K.; Natarajan, T.S. Influence of TiO_2 morphology on the photocatalytic efficiency of direct Z-scheme g-C_3N_4/TiO_2 photocatalysts for isoniazid degradation. *Chem. Eng. J.* **2015**, *281*, 549.
42. Cho, K.; Biswas, P.; Fraundorf, P. Characterization of nanostructured pristine and Fe-and V-doped titania synthesized by atomization and bubbling. *J. Ind. Eng. Chem.* **2014**, *20*, 558.
43. Zhu, S.; Li, Y.; Fan, C.; et al. Structural studies of iron-doped TiO_2 nano-composites by Mössbauer spectroscopy, X-ray diffraction and transmission microscopy. *Phys. B* **2005**, *364*, 199.
44. Fan, W.Q.; Bai, H.Y.; Zhang, G.H.; et al. Titanium dioxide macroporous materials doped with iron: Synthesis and photo-catalytic properties. *CrystEngComm* **2014**, *16*, 116.
45. Wang, Z.M.; Yang, G.; Biswas, P.; et al. Processing of iron-doped titania powders in flame aerosol reactors. *Powder Technol.* **2001**, *114*, 197.
46. Post, J.E.; Buchwald, V.F. Crystal structure refinement of akaganeite. *Am. Mineral.* **1991**, *76*, 272.
47. Yu, Y.L.; Wang, X.L.; Sun, H.Y.; et al. 3D anatase TiO_2 hollow microspheres assembled with high-energy {001} facets for lithium-ion batteries. *RSC Adv.* **2012**, *2*, 7901.
48. Dai, G.P.; Liu, S.Q.; Liang, Y.; et al. A simple preparation of carbon and nitrogen co-doped nanoscaled TiO_2 with exposed {001} facets for enhanced visible-light photocatalytic activity. *J. Mol. Catal. A-Chem.* **2013**, *368–369*, 38.
49. Han, X.; Kuang, Q.; Jin, M.; et al. Synthesis of titania nanosheets with a high percentage of exposed (001) facets and related photocatalytic properties. *J. Am. Chem. Soc.* **2009**, *131*, 3152.
50. Liu, M.; Piao, L.; Zhao, L.; et al. Anatase TiO_2 single crystals with exposed {001} and {110} facets: facile synthesis and enhanced photocatalysis. *Chem. Comm.* **2010**, *46*, 1664.
51. Song, X.; Boily, J.F. Competitive ligand exchange on akaganéite surfaces enriches bulk chloride loadings. *J. Colloid. Interface Sci.* **2012**, *376*, 331.
52. Morcillo, M.; Alcántara, J.; Díaz, I.; et al. Corrosión atmosférica marina de aceros al carbono. *Rev. Metal.* **2015**, *51*, e045.
53. Li, J.; Zeng, H.C. Hollowing Sn-doped TiO_2 nanospheres via Ostwald ripening. *J. Am. Chem. Soc.* **2007**, *129*, 15839.
54. Xu, R.; Zeng, H.C. Self-generation of tiered surfactant superstructures for one-pot synthesis of Co_3O_4 nanocubes and their close-and non-close-packed organizations. *Langmuir* **2004**, *20*, 9780.
55. Chang, Y.; Lye, M.L.; Zeng, H.C. Large-scale synthesis of high-quality ultralong copper nanowires. *Langmuir* **2005**, *21*, 3746.
56. Xu, M.; Da, P.; Wu, H.; et al. Controlled Sn-doping in TiO_2 nanowire photoanodes with enhanced photoelectrochemical conversion. *Nano Lett.* **2012**, *12*, 1503.

57. Zhu, J.; Chen, F.; Zhang, J.; et al. Fe^{3+}-TiO_2 photocatalysts prepared by combining sol–gel method with hydrothermal treatment and their characterization. *J. Photochem. Photobiol. A-Chem.* **2006**, *180*, 196.
58. Teo, S.H.; Zeng, H.C. Surface and textural properties of network-modified silica as a function of transition metal dopant zirconium. *J. Phys. Chem. B* **2001**, *105*, 9093.
59. Tong, T.; Zhang, J.; Tian, B.; et al. Preparation of Fe^{3+}-doped TiO_2 catalysts by controlled hydrolysis of titanium alkoxide and study on their photocatalytic activity for methyl orange degradation. *J. Hazard. Mater.* **2008**, *155*, 572.
60. Wang, Y.M.; Liu, S.W.; Lü, M.K.; et al. Preparation and photocatalytic properties of Zr^{4+}-doped TiO_2 nanocrystals. *J. Mol. Catal. A-Chem.* **2004**, *215*, 137.
61. Lukáč, J.; Klementova, M.; Bezdička, P.; et al. Influence of Zr as TiO_2 doping ion on photocatalytic degradation of 4-chlorophenol. *Appl. Catal. B-Environ.* **2007**, *74*, 83.
62. Burdett, J.K.; Hughbanks, T.; Miller, G.J., Jr.; et al. Structural-electronic relationships in inorganic solids: powder neutron diffraction studies of the rutile and anatase polymorphs of titanium dioxide at 15 and 295 K. *J. Am. Chem. Soc.* **1987**, *109*, 3639.
63. Fan, W.Q.; Bai, H.Y.; Zhang, G.H.; et al. Titanium dioxide macroporous materials doped with iron: Synthesis and photo-catalytic properties. *CrystEngComm* **2014**, *16*, 116.
64. Wang, Z.M.; Yang, G.; Biswas, P.; et al. Processing of iron-doped titania powders in flame aerosol reactors. *Powder Technol.* **2001**, *114*, 197.
65. Reddy, J.K.; Lalitha, K.; Reddy, P.V.L.; et al. Fe/TiO_2: A visible light active photocatalyst for the continuous production of hydrogen from water splitting under solar irradiation. *Catalysis Lett.* **2014**, *144*, 340.
66. Xu, Z.; Yu, J. Visible-light-induced photoelectrochemical behaviors of Fe-modified TiO_2 nanotube arrays. *Nanoscale* **2011**, *3*, 3138.
67. Delekar, S.D.; Yadav, H.M.; Achary, S.N.; et al. Structural refinement and photocatalytic activity of Fe-doped anatase TiO_2 nanoparticles. *Appl. Surf. Sci.* **2012**, *263*, 536.
68. Xu, A.W.; Gao, Y.; Liu, H.Q. The preparation, characterization, and their photocatalytic activities of rare-earth-doped TiO_2 nanoparticles. *J. Catal.* **2002**, *207*, 151.
69. Hsutomu, H.; Nosaka, Y. Properties of $O_2^{\bullet-}$ and $OH^{\bullet}$ formed in TiO_2 aqueous suspensions by photocatalytic reaction and the influence of H_2O_2 and some ions. *Langmuir* **2002**, *18*, 3247.
70. Yu, J.C.; Yu, J.; Ho, W.; et al. Effects of F-doping on the photocatalytic activity and microstructures of nanocrystalline TiO_2 powders. *Chem. Mater.* **2002**, *14*, 3808.
71. Zhu, J.; Zhang, J.; Chen, F.; et al. High activity TiO_2 photocatalysts prepared by a modified sol–gel method: characterization and their photocatalytic activity for the degradation of XRG and X-GL. *Topic. Catalysis* **2005**, *35*, 261.
72. Liu, M.; Piao, L.; Zhao, L.; et al. Anatase TiO_2 single crystals with exposed {001} and {110} facets: facile synthesis and enhanced photocatalysis. *Chem. Commun.* **2010**, *46*, 1664.
73. Thimsen, E.; Biswas, S.; Lo, C.S.; Biswas, P. Predicting the band structure of mixed transition metal oxides: theory and experiment. *J. Phys. Chem. C* **2009**, *113*, 2014.
74. Wang, C.Y.; Böttcher, C.; Bahnemann, D.W.; et al. A comparative study of nanometer sized Fe(III)-doped TiO_2 photocatalysts: synthesis, characterization and activity. *J. Mater. Chem.* **2003**, *13*, 2322.
75. Niu, Y.; Xing, M.; Zhang, J.; Tian, B. Visible light activated sulfur and iron co-doped TiO_2 photocatalyst for the photocatalytic degradation of phenol. *Catal. Today* **2013**, *201*, 159.
76. Carneiro, J.O.; Azevedo, S.; Fernandes, F.; et al. Synthesis of iron-doped TiO_2 nanoparticles by ball-milling process: the influence of process parameters on the structural, optical, magnetic, and photocatalytic properties. *J. Mater. Sci.* **2014**, *49*, 7476.
77. Zhang, Z.; Wang, C.C.; Zakaria, R.; Ying, J.Y. Role of particle size in nanocrystalline TiO_2-based photocatalysts. *J. Phys. Chem. B* **1998**, *102*, 10871.
78. Zhu, J.; Chen, F.; Zhang, J.; et al. Fe^{3+}-TiO_2 photocatalysts prepared by combining sol–gel method with hydrothermal treatment and their characterization. *J. Photoch. Photobio. A* **2006**, *180*, 196.
79. Liu, Z.; Ran, H.; Niu, J.; et al. One-pot synthesis of bismuth oxyhalide/oxygen-rich bismuth oxyhalide Heterojunction and its photocatalytic activity. *J. Colloid Interf. Sci.* **2014**, *431*, 187.
80. He, D.; Chen, M.; Teng, F.; et al. Enhanced cyclability of CdS/TiO_2 photocatalyst by stable interface structure. *Superlattice. Microstruct.* **2012**, *51*, 799.
81. Liu, L.; Gu, X.; Sun, C.; et al. In situ loading of ultra-small Cu_2O particles on TiO_2 nanosheets to enhance the visible-light photoactivity. *Nanoscale* **2012**, *4*, 6351.
82. Hou, J.; Yang, C.; Wang, Z.; et al. Bi_2O_3 quantum dots decorated anatase TiO_2 nanocrystals with exposed {001} facets on graphene sheets for enhanced visible-light photocatalytic performance. *Appl. Catal. B-Environ.* **2013**, *129*, 333.

83. Liu, Z.; Sun, D.D.; Guo, P.; Leckie, J.O. An efficient bicomponent TiO_2/SnO_2 nanofiber photocatalyst fabricated by electrospinning with a side-by-side dual spinneret method. *Nano Lett.* **2007**, *7*, 1081.
84. Jiang, D.; Zhang, S.; Zhao, H. Photocatalytic degradation characteristics of different organic compounds at TiO_2 nanoporous film electrodes with mixed anatase/rutile phases. *Environ*. *Sci. Technol.* **2007**, *41*, 303.
85. Liu, B.; Khare, A.; Aydil, E.S. TiO_2–B/anatase core–shell heterojunction nanowires for photocatalysis. *ACS Appl. Mater. Inter.* **2011**, *3*, 4444.
86. Guo, E.; Yin, L. Tailored $SrTiO_3/TiO_2$ heterostructures for dye-sensitized solar cells with enhanced photoelectric conversion performance. *J. Mater. Chem. A* **2015**, *3*, 13390–13401.
87. Scanlon, D.O.; Dunnill, C.W.; Buckeridge, J.; et al. Band alignment of rutile and anatase TiO_2. *Nat. Mater.* **2013**, *12*, 798.
88. Cao, Y.; He, T.; Chen, Y.; Cao, Y. Fabrication of rutile TiO_2-Sn/anatase TiO_2-N heterostructure and its application in visible-light photocatalysis. *J. Phys. Chem. C* **2010**, *114*, 3627.
89. Hensel, J.; Wang, G.; Li, Y.; Zhang, J.Z. Synergistic effect of CdSe quantum dot sensitization and nitrogen doping of TiO_2 nanostructures for photoelectrochemical solar hydrogen generation. *Nano. Lett.* **2010**, *10*, 478.
90. Pian, X.; Lin, B.; Chen, Y.; et al. Pillared nanocomposite TiO_2/Bi-doped hexaniobate with visible-light photocatalytic activity. *J. Phys. Chem. C* **2011**, *115*, 6531.
91. Zhu, J.; Zach, M. Nanostructured materials for photocatalytic hydrogen production. *Curr*. *Opin. Colloid Interface Sci.* **2009**, *14*, 260.
92. Leland, J.K.; Bard, A.J. Photochemistry of colloidal semiconducting iron oxide polymorphs. *J. Phys. Chem.* **1987**, *91*, 5076.
93. White, A.F. Rev. Heterogeneous electrochemical reactions associated with oxidation of ferrous oxide and silicate surfaces. *Mineral. Geochem.* **1990**, *23*, 467.
94. Chowdhury, M.; Ntiribinyange, M.; Nyamayaro, K.; Fester, V. Photocatalytic activities of ultra-small β-FeOOH and TiO_2 heterojunction structure under simulated solar irradiation. *Mater*. *Res. Bull.* **2015**, *68*, 133.
95. Pradel, J.; Castillo, S.; Traverse, J.P.; et al. Ferric hydroxide oxide from the goethite process: characterization and potential use. *Ind*. *Eng. Chem. Res.* **1993**, *32*, 1801.
96. Zhang, Z.; Wang, W.; Wang, L.; Sun, S. Enhancement of visible-light photocatalysis by coupling with narrow-band-gap semiconductor: a case study on Bi_2S_3/Bi_2WO_6. *ACS Appl*. *Mater. Inter.* **2012**, *4*, 593.
97. Rawal, S.B.; Bera, S.; Lee, D.; et al. Design of visible-light photocatalysts by coupling of narrow bandgap semiconductors and TiO_2: Effect of their relative energy band positions on the photocatalytic efficiency. *Catal*. *Sci. Technol.* **2013**, *3*, 1822.